International Journal of Naval Architecture and Ocean Engineering 13 (2021) 718–733

Contents lists available at ScienceDirect

International Journal of Naval Architecture and Ocean Engineering

journal homepage: http://www.journals.elsevier.com/international-journal-of-naval-architecture-and-ocean-engineering/

Experimental study of internal solitary wave loads on the semi-submersible platform

Jingjing Zhang [a, b], Yi Liu [c], Ke Chen [a, b, *], Yunxiang You [a, b], Jinlong Duan [d]

[a] State Key Laboratory of Ocean Engineering, Shanghai Jiao Tong University, Shanghai, China
[b] Yazhou Bay Institute of Deep sea Technology, Shanghai Jiao Tong University, Sanya, China
[c] Marine Design & Research Institute of China, Shanghai, China
[d] Key Laboratory for Mechanics in Fluid Solid Coupling Systems, Institute of Mechanics, Chinese Academy of Sciences, Beijing, China

ARTICLE INFO

Article history:
Received 23 November 2020
Received in revised form
15 July 2021
Accepted 12 August 2021
Available online 26 August 2021

Keywords:
Morison equation
ISWs
Semi-submersible
Model tests
Froude-Krylov forces

ABSTRACT

A prediction method, based on the Morison equation as well as Froude-Krylov formula, is presented to simulate the loads acting on the columns and caissons of the semi-submersible platform induced by Internal Solitary Wave (ISW) respectively. Combined with the experimental results, empirical formulas of the drag and inertia coefficients in Morison equation can be determined as a function of the Keulegan −Carpenter (KC) number, Reynolds number (Re) and upper layer depth h_1/h respectively. The experimental and calculated results are compared. And a good agreement is observed, which proves that the present prediction method can be used for analyzing the ISW-forces on the semi-submersible platform. Moreover, the results also demonstrate the layer thickness ratio has a significant effect upon the maximum horizontal forces on the columns and caissons, but both minimum horizontal and vertical forces are scarcely affected. In addition, the incoming wave directions may also contribute greatly to the values of horizontal forces exerted on the caissons, which can be ignored in the vertical force analysis.

1. Introduction

Due to the lack of the resources in shallow water, gas and oil exploration has moved towards the deep-water region, which can be severely affected by the environmental condition, including Internal Solitary W aves (ISWs). Most of the ISWs propagate at the interface between the thermocline and the deep sea, which is mainly thought to be generated by tidally driven flows over bottom topography (Goryachkin et al., 1992; Lamb, 1994). ISWs with large amplitudes and low frequency can induce strong convergence and divergence of velocity. In addition, unsteady change can occur temporally and spatially for ISWs with large amplitudes and low frequency during the propagation in oceans (Hutter, 2012). Such hidden giant ISWs can intensify the enormous energy exchange between the upper and lower layers of oceans (Leichter et al., 2005; Zhang et al., 2014), which may exert catastrophic forces on the offshore structures and underwater vehicles in the operation (Bole et al., 1994; Ebbesmeyer et al., 1991; Osborne and Burch, 1980; CHEN, 1996). Therefore, it is of significant importance to understand the impact of ISWs forces on the oceanic engineering structures, so as to further investigate on what methods can be taken to reduce such disadvantages.

Since KdV theory has performed better than expected under many types of tests in 1981 (Koop and Butler, 1981), particular interest has recently been devoted to ISWs propagating phenomena and wave loads on offshore structures. Kao et al. (1985) conducted experimental study on ISWs propagation on the slope, and found that shear instability began to appear on the backside of the waves, with turbulent mixing sometimes occurring afterwards. Chen et al. (2007) performed a stratification laboratory experiment in a wave flume, then compared the main behaviors between depression and elevation type of the ISW when it propagated over a steep slope. Cai et al. (2003; 2006; 2008a) introduced the Morison equation and the modal separation method to investigate the characteristics of forces and torques that are exerted by ISWs on a small-scale pile and discussed the influence of shear flows on the corresponding actions. Xie et al. (2010; 2011) presented a series of experimental results, focusing on the time dependent ISW-loads on the cylindrical pile in two-dimensional flow based on the full Euler equation

* Corresponding author. State Key Laboratory of Ocean Engineering, Shanghai Jiao Tong University, Shanghai, China.
E-mail address: eaulphan@sjtu.edu.cn (K. Chen).
Peer review under responsibility of The Society of Naval Architects of Korea.

https://doi.org/10.1016/j.ijnaoe.2021.08.002

and MCC theory. Huang et al. (2013) experimentally described the mechanism of interaction between ISWs and the semi-submersible platform under the condition of the incoming waves, and obtained that the vertical load is mainly Froude-Krylov force which can be computed by integrating the ISW-induced dynamic press over surfaces of caissons, while the horizontal forces consist of drag and inertia components which can be estimated by using Morison equation. Moreover, numerical models are also employed to study the loads exerted by ISWs on marine structures. Wang et al. (2015) calculated the loads associated with ISWs on a semi-submersible platform based on numerical simulation and the Navier-Stokes equation. You et al. (2010; 2012) established a time-domain numerical model to detail the action of ISWs on the semi-submersible and the tension leg platform using them KdV theory by combining the Morison and coupling motion equation of six degrees of freedom. Although plenty of works have been carried out, the effect of the direction of incoming waves on the calculation of forces exerted by ISWs is still not thoroughly understood, as well as the selection of the hydrodynamic coefficients in Morison equation. So far, only Wang et al. (2020) have experimentally studied how different incident angles of the ISWs impact on the forces acting on the submerged slender body. Therefore, much more attentions should be paid on the prediction method of the ISWs on the columns and caissons of the more widely used 4-columns classic semi-submersible platform independently.

The aim of this study is to propose a prediction method of ISW-induced force acting on the columns and caissons of the semi-submersible platform respectively. The prediction method is firstly verified based on the experimental data and the calculated results. In addition, expanded formulas are proposed with the definitions of the key parameters C_m and C_d in Morison equation being discussed thereafter. The paper is organized as follows. Section 2 describes the ISWs theories and ISW-loads. Section 3 gives a brief description of experimental set-up, including the flume, the conductivity probes, the two-layer system, the test model and the three-component force transducer. In Section 4, empirical formulas of the drag and inertia coefficients are established from the experimental data; the measured forces are compared with the computed results based on the prediction method and the effects of the amplitudes, layer thickness ratios and incoming wave directions are discussed. Conclusions are drawn in the last section.

2. Summary of previous theoretical results

2.1. ISWs theoretical models

A one-dimensional ISW propagating along the interface between two homogeneous incompressible and inviscid fluid of different density is considered. The applicability of the KdV equation dealing with weakly nonlinear waves has been extensively tested against experimental data (Michallet and Barthélemy, 1997). KdV theory for ISWs is given in two-layer form as follows (Osborne and Burch, 1980):

$$\zeta_{\mathrm{KdV}} = -a\,\mathrm{sech}^2\left(\frac{x - c_{\mathrm{KdV}}t}{\lambda_{\mathrm{KdV}}}\right) \tag{1}$$

Here ζ describes a displacement of the interface in the coordinate system where the fluid motion appears steady, a is the amplitude. The negative sign indicates that this is a depression wave, as would be the case when the upper layer depth h_1 is less than the lower layer depth h_2. $\lambda_{\mathrm{KdV}} = \sqrt{12c_2/ac_1}$ provides a length scale for the solitary wave and c_{KdV} is the phase velocity. The ISW propagates without change of shape at constant speed c_{KdV} defined by Choi and Camassa (1999):

$$c_{KdV} = c_0\left(1 - \frac{ac_1}{3c_0}\right)$$
$$c_0 = \sqrt{\frac{gh_1h_2(\rho_2 - \rho_1)}{\rho_1h_2 + \rho_2h_1}}, c_1 = -\frac{3c_0}{2}\frac{\rho_1h_2^2 - \rho_2h_1^2}{\rho_1h_1h_2^2 + \rho_2h_1^2h_2}, c_2 = \frac{c_0}{6}\frac{\rho_1h_2h_1^2 + \rho_2h_1h_2^2}{\rho_1h_2 + \rho_2h_1} \tag{2}$$

where c_0 is the linear long-wave velocity, c_1 is the coefficient of the nonlinear term and c_2 represents the coefficient of nonlinear dispersive terms.

For a sufficiently large-amplitude soliton, one may reason that, the dynamic balance between the nonlinear and dispersive terms is no longer maintained in the governing equation, which makes the KdV equation unsuitable for describing large amplitude ISWs. One way to overcome this is by inclusion of the cubic nonlinearity (Djordjevic and Redekopp, 1978; Kakutani and Yamasaki, 1978), which is eKdV (extended KdV) equation:

$$\zeta_t + \left(c_0 + c_1\zeta + c_3\zeta^2\right)\zeta_x + c_2\zeta_{xxx} = 0 \tag{3}$$

For the incompressible two-layer fluid with a rigid lid, in the Boussinesq approximation (Helfrich and Melville, 2006)

$$c_3 = \frac{3c_0}{h_1^2h_2^2}\left[\frac{7}{8}\left(\frac{\rho_1h_2^2 - \rho_2h_1^2}{\rho_1h_2 + \rho_2h_1}\right)^2 - \frac{\rho_1h_2^3 + \rho_2h_1^3}{\rho_1h_2 + \rho_2h_1}\right] \tag{4}$$

Theoretical solutions to the eKdV equation can be expressed in different forms (Helfrich and Melville, 2006), one of which is

$$\zeta_{\mathrm{eKdV}} = \frac{\mathrm{a}}{b + (1-b)\cosh^2[\lambda_{eKdV}(x - c_{eKdV}t)]}$$
$$b = \frac{-ac_3}{2c_1 + ac_3} \tag{5}$$

with the phase velocity of theoretical solution c_{eKdV} and the characteristic length of the solitary wave λ_{eKdV} being

$$c_{eKdV} = c_0 + \frac{a}{3}\left(c_1 + \frac{1}{2}ac_3\right), \quad \lambda_{eKdV}^2 = \frac{a\left(c_1 + \frac{1}{2}ac_3\right)}{12c_2} \tag{6}$$

Based on the continuity equation and original Euler equations, an expression by an ordinary differential equation is derived for strongly nonlinear waves, which is MCC (Miyata- Choi- Camassa) equation (Choi and Camassa, 1999; Miyata, 1985):

$$(\zeta_x)^2 = \left[\frac{3g(\rho_2-\rho_1)}{c_{MCC}^2\left(\rho_1 h_1^2 - \rho_2 h_2^2\right)}\right] \frac{\zeta^2(\zeta-a_-)(\zeta-a_+)}{\zeta-a_*} \tag{7}$$

where a_* is given by

$$a_* = -\frac{h_1 h_2(\rho_1 h_1 + \rho_2 h_2)}{\rho_1 h_1^2 - \rho_2 h_2^2} \tag{8}$$

And $a_\pm$ are the two roots of a quadratic equation

$$\zeta^2 + q_1\zeta + q_2 = 0 \tag{9}$$

With q_1 and q_2 defined by

$$q_1 = -\frac{c_{MCC}^2}{g} - h_1 + h_2, \quad q_2 = h_1 h_2\left(\frac{c_{MCC}^2}{c_0^2} - 1\right) \tag{10}$$

Here c_{MCC} is the phase speed, which can be written in terms of a as

$$\frac{c_{MCC}^2}{c_0^2} = \frac{(h_1-a)(h_2+a)}{h_1 h_2 - (c_0^2/g)a} \tag{11}$$

The relation between dispersion and nonlinearity, given by the following forms (Huang et al., 2013), may be used to determine the applicable conditions for different ISW theories.

1. MCC theory is applicable when $\mu < \mu_0, \varepsilon > \sqrt{\mu}$ or $\mu > \mu_0$;
2. eKdV theory is applicable when $\mu < \mu_0$ and $\mu < \varepsilon < \sqrt{\mu}$;
3. KdV theory is applicable when $\mu < \mu_0$ and $\varepsilon < \mu$;

Where $\mu = (h/\lambda)^2$ is the dispersion parameter, $\varepsilon = |a|/h$ is the nonlinearity parameter, and $\mu_0 = 0.1$ is the critical dispersion parameter.

And some wave profiles recorded from the array of the conductive probes are compared with KdV, eKdV and MCC theories, as shown in Fig. 1. From the figure, it is seen that the KdV profile is the narrowest one under the same amplitude. For a small depression ISW, the experimental results agree with the KdV equation. Obviously, the moderate-amplitude ISWs fit better with the eKdV equation. For the strong nonlinear ISW, it is closer to the MCC theory.

2.2. ISW-loads

Morison equation is an empirical formula which is normally applied to the structures that are small compared to the wave length. Generally, the characteristic wavelength of ISWs is over the range hundreds of meters to a few kilometers, while the columns of the semi-submersible platform with characteristic diameters are normally less than 20 m. Under the condition that characteristic length of semi-submersible platform D_e relative to the wavelength L is less than 0.15, the incident wave field is not disturbed as if the platform does not exist, permitting one to use Morison equation as

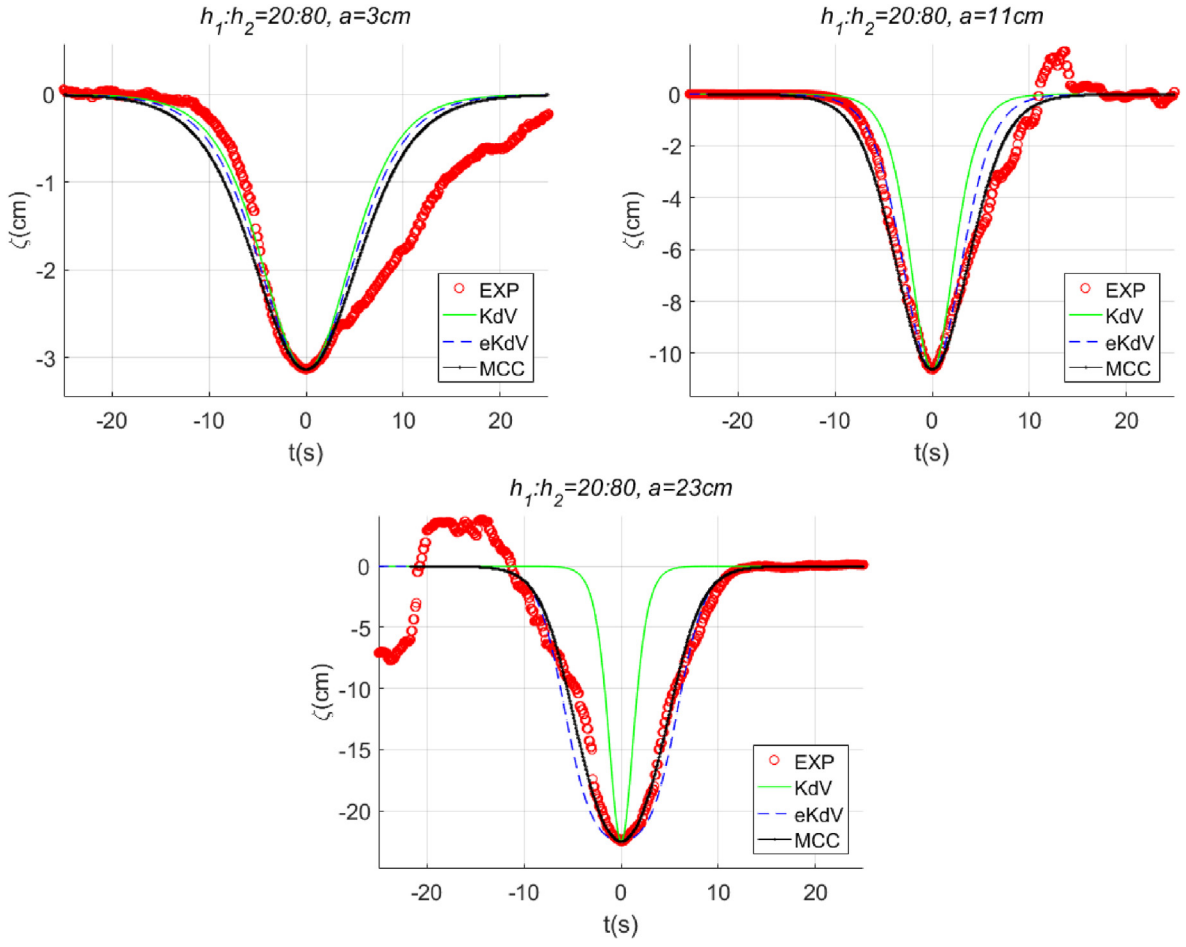

Fig. 1. Wave profiles under different amplitudes.

an approximation to compute the forces associated with ISWs on the platform. Morison equation expressed the wave force to be composed of inertia and drag forces linearly added together, given as (Morison et al., 1950)

$$F_{col}=\sum_{i=1}^{N_{col}}F_i=\rho C_m\sum_{i=1}^{N_{col}}(S_{col})_i\frac{\partial V_i}{\partial t}+\frac{1}{2}\rho C_d\sum_{i=1}^{N_{col}}(D_{col})_i|V_i|V_i \tag{12}$$

Here, N_{col} is number of the vertical column unit, $(S_{col})_i$ is cross-sectional area of the i-th column at different vertical location, $(D_{col})_i$ is the equivalent diameter of the column, V_i and $\partial V_i/\partial t$ are horizontal fluid velocity and acceleration normal to the i-th column, respectively.

For the two-layer fluid simulation, water is assumed as an incompressible, irrotational fluid. The horizontal fluid velocity V_i exerted by ISWs is decomposed into transient horizontal u_j and transient vertical velocities w_j, which can be determined by (Camassa et al., 2006)

$$\begin{aligned}u_j(x,z,t)&=\overline{u}_j(x,t)+\left[\frac{\overline{h}_j^2}{6}+\frac{\left(z+(-1)^j h_j\right)^2}{2}\right]\overline{u}_{jxx}(x,t)\\ w_j(x,z,t)&=(-1)^{j+1}\left[h_j+(-1)^j z\right]\overline{u}_{jx}(x,t)\end{aligned} \tag{13}$$

In which $\overline{h}_j=h_j+(-1)^j\zeta,\ (j=1,\ 2)$ is the undisturbed thickness of the fluid layer; $\overline{u}_j$ is the layer-averaged velocity of two different layers and subscripts are the derivative of the variable with respect to 'x':

$$\begin{aligned}\overline{u}_{jx}&=\frac{d\overline{u}_j}{dx},\overline{u}_{jxx}=\frac{d^2\overline{u}_j}{dx^2}\\ \overline{u}_1&=-c\frac{\zeta}{h_1-\zeta},\overline{u}_2=c\frac{\zeta}{h_2+\zeta}\end{aligned} \tag{14}$$

Here, c is the phase velocity of an ISW; ζ is the interface displacement that can be expressed by KdV, eKdV and MCC theories.

For simplicity, the density of the two-layer fluid, transient horizontal and vertical velocities are expressed by the following forms:

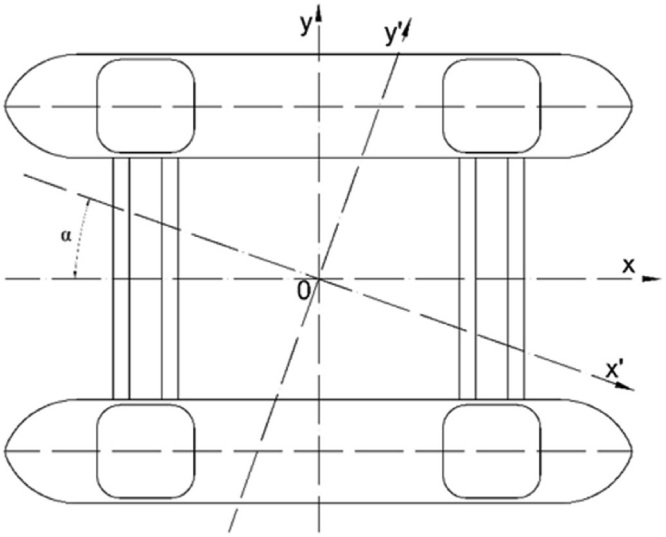

Fig. 2. Reference coordinate systems.

$$u=\begin{cases}u_1,\zeta<z<h_1\\ u_2,-h_2<z<\zeta\end{cases},\ w=\begin{cases}w_1,\zeta<z<h_1\\ w_2,-h_2<z<\zeta\end{cases},\ \rho=\begin{cases}\rho_1,\zeta<z<h_1\\ \rho_2,-h_2<z<\zeta\end{cases} \tag{15}$$

Note that the caissons of the platform are the horizontal structures submerged in water, which is not only subjected to the ISWs horizontal forces, but also to the vertical pressures. And the force analysis is also owing to the effect of the incident wave direction. When the propagation direction of the ISWs is parallel to the longitudinal profile of the platform, the caissons are only subjected to the differential pressure of the main body in the horizontal direction, which can be estimated by means of the Froude-Krylov approach (Huang et al., 2013). Once the wave propagating is not parallel to the longitudinal profile, the ISWs-forces assume to be mainly composed of drag and inertia forces, and the modified Morison equation for the wave force estimation is more appropriate to be considered. A reference coordinate system transformation in regard to the incident angle α is established, as shown in Fig. 2. Consider the coordinate system xoy as the initial fixed reference coordinate under the condition that the propagation direction of the ISWs is parallel to the longitudinal profile of the platform, and another coordinate system $x'oy'$ can be obtained after clockwise rotating coordinate system xoy to α degrees. Set (x,y) for a point on the platform in coordinate system xoy, and coordinate (x',y') can be obtained in coordinate system $x'oy'$ by using rotation transformation

$$\begin{aligned}x'&=x\cos\alpha-y\sin\alpha\\ y'&=y\cos\alpha+x\sin\alpha\\ z'&=z\end{aligned} \tag{16}$$

Under the condition of the incident angle α, the drag and inertia forces acting on the caissons as well as the Froude-Krylov force in the x' and y' directions can be written as (Faltinsen, 1993)

$$\begin{aligned}F_{cax}(X')&=\sum_{k=1}^{N_{ca}}(f_{Ica}(X',z')+f_{Dca}(X',z'))+\sum_{k=1}^{N_{pan}}p\mathrm{n_k}\cdot\mathrm{e_1}ds_{ca}\\ F_{cay}(X')&=\sum_{k=1}^{N_{pan}}p\mathrm{n_k}\cdot\mathrm{e_2}ds_{ca}\end{aligned} \tag{17}$$

With

$$\begin{aligned}f_{Ica}(X',z')&=\rho S_{ca}C_{\mathrm{mca}}\frac{\partial u(X',z')_{ca}}{\partial t}dl_{ca}\sin\alpha\\ f_{Dca}(X',z')&=\frac{1}{2}\rho D_{ca}C_{\mathrm{dca}}U_{ca}u(X',z')_{ca}dl_{ca}\sin\alpha\\ U_{ca}&=\sqrt{u(X',z')_{ca}^2+w(X',z')_{ca}^2}\end{aligned} \tag{18}$$

where $F_{cax}(X')$ and $F_{cay}(X')$ are forces acting on the caisson in the x' and y' directions, respectively; $f_{Ica}(X',z')$ and $f_{Dca}(X',z')$ are inertia force and drag force acting on the element of the caisson respectively; $u(X',z')_{ca}$, $w(X',z')_{ca}$ and $\partial u(X',z')/\partial t$ are the horizontal velocity, vertical velocity and horizontal acceleration at the central point of the caisson unit, respectively; N_{ca} is the number of the caisson unit; N_{pan} is the number of panels on the surface of the caisson; dS_{ca} is the area of the panel; n_k is inner unit normal vector of the k-th panel; e_1 and e_2 are unit vector in the x' and y' directions; S_{ca} is the sectional area of the caisson; D_{ca} is the height of the caisson; dl_{ca} is the element length of the caisson.

Of particular concern is that no matter whether the propagation direction of the ISWs is parallel to the longitudinal profile of the platform, the vertical forces could be obtained by integrating the

dynamic pressure over the upper and lower surfaces of the caissons, that is, the Froude-Krylov force (Huang et al., 2013), which is due to the neglect of interaction between caissons and ISWs in the governing equation.

$$F_p = \sum_{k=1}^{N_{ca}} \iint_{S_k} p n_k ds \tag{19}$$

where p is the dynamic pressure in the fluid field,S_k is the upper and lower surfaces of the *k-th* caisson and n_k is the unit normal vector of the upper and lower surfaces. The dynamic pressure p can be derived from Bernoulli formula:

$$p = -\rho_1 \left[c u_j + \frac{1}{2}\left(u_j^2 + w_j^2\right)\right] \tag{20}$$

3. Experimental methods

Four different thickness ratios of layers are considered in the experiments. And the investigation is comprised of two parts. The experiments with three layer thickness ratios ($h_1 : h_2 = 20 : 80, 25 : 75, 30 : 70$), were carried out in order to study the characteristic of loads induced by ISWs exerted on the columns and caissons of the semi-submersible platform respectively. While the experiments under the layer thickness ratio $h_1 : h_2 = 35 : 65$ were conducted to verify the applicability of the prediction method.

The experiments were performed in the density stratified wave flume of 30 m long, 0.6 m wide and 1.2 m deep to obtain the forces exerting on the columns and caissons of the semi-submersible platform due to ISWs. The stratified fluid is obtained by filling the flume with two-layer fluids, which consists of an upper fresh water layer and a lower salt water layer with a thin transition region at interface. Before running the experimental cases, the upper layer is filled with fresh water ($\rho_1 = 998\text{kg/m}^3$) to a desired depth h_1, and then the brine water ($\rho_2 = 1025\text{kg/m}^3$) is pumped slowly below the lighter water through several openings along the base of the flume until the total water depth h reaches 1 m. After the stratification appears in the flume, the vertical density distribution of the fluid can be measured with a probe that could move along the vertical direction. To satisfy the accuracy requirement, the measuring point interval in the vicinity of the interface is maintained at 0.5 cm, and the typical density can be obtained. Fig. 3 (left) shows the typical density profiles under layer thickness ratio $h_1 : h_2 = 20 : 80$. The buoyancy frequency of the stratified fluid is also depicted in Fig. 3 (right), in which a narrow pycnocline with a thickness of 2–3 cm can be seen. The peak of the buoyancy frequency profile is considered the characteristic value for the fluid system, that is, the maximum value of the buoyancy frequency is regarded as at the interface between the upper and lower layer. The buoyancy frequency is defined as $N = \sqrt{(g/\rho_1)(\partial\rho_z/\partial z)}$ (ρ_z is the density, g is the gravitational acceleration and z is the vertical coordinate).

A rough sketch of the experimental set-up is presented in Fig. 4, which consists of three regions: the wave generated, propagation and dissipation regions. High-quality ISWs can be generated by an effective wave-maker of double-plate type (identified by black), which is similar to the mechanism as described in the previous paper (Wessels and Hutter, 1996). The wave-maker mainly consists of two vertical steel panels with the same heights as the upper and lower depths of the undisturbed fluid, respectively. Under the control of the computer terminal, the two panels are simultaneously advanced in opposite directions at pre-calculated velocities, so as to generate a steady ISW of depression at the interface of the two layers. And nonlinear ISWs with different amplitudes can be generated by adjusting the speed of the two plates. In addition, a steel plate is arranged on the top of the wave maker to reduce the disturbance of the free surface, avoiding changing the waveform in the process of propagation. A wedge-shape wave absorber is fixed at the left end of the flume, namely the wave dissipation region, to maximally prevent waves from reflecting on the work region.

Two arrays of conductivity probes are mounted on one side of the flume with a horizontal separation distance of 3 m to monitor the shape and speed of the ISW as it passes along the tank. Each array includes 9 conductivity probes ranging along the vertical direction with 3 cm intervals between adjacent probes. The phase velocity of the ISW could be estimated from the signal of two conductivity probes, which can be deduced from the distance between the two probes and the time lapse at which the maxima of the two corresponding signals pass them. Fig. 5 shows the measurement results of the typical depression ISW waveform for different incident wave amplitudes under $h_1 : h_2$ being 20 : 80. From the figure, the waveform of an ISW with small amplitude appears weak oscillations at trailing waves, which is caused by the wave scattering when it propagates in the inhomogeneous medium. As the amplitudes increase, the obvious oscillatory suggests that incident ISWs with larger amplitude create stronger disturbance.

The schematic diagram of the semi-submersible platform model with a 1:300 scale in the experiment set-up is shown in Fig. 6(a). The test model consists of 4 columns with a 0.062 m × 0.062 m cross-section, 4 horizontal braces with diameter of 0.02 m and 2 caissons of 0.414 m long. The forces on the columns and caissons of

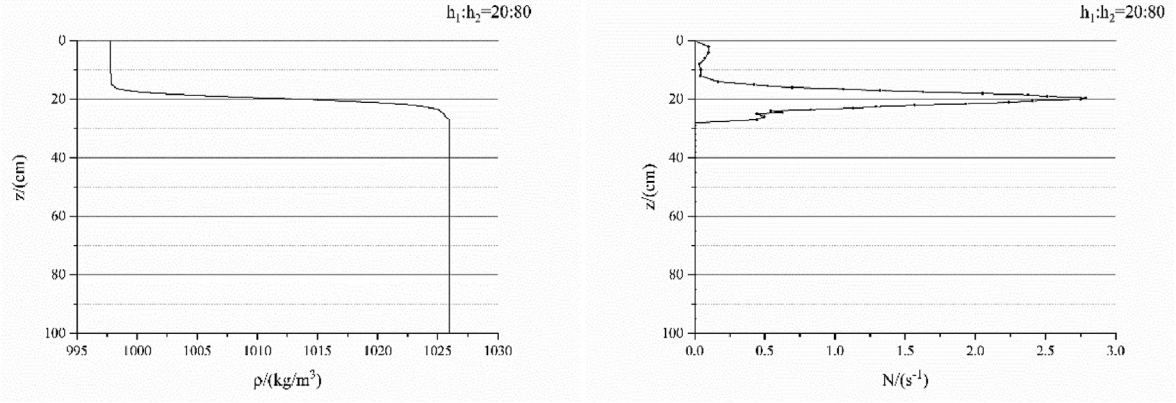

Fig. 3. The density profile (left) and vertical distribution of the buoyancy frequency (right).

the model during the ISW propagation are measured by using a specially designed force measurement device, which contains two force balances, a signal acquisition and processing system. In order to ensure the forces on the columns and caissons are measured simultaneously, a two-component force dynamometer is directly installed on the columns for measuring the horizontal forces along the longitudinal or transversal direction of the tank acted on the columns, as shown in Fig. 6(b). Meanwhile, the three-component force measurement sensor is connected with the caissons through a piece of organic glass plate and four screws, which is used to gauge the longitudinal and transversal horizontal forces as well as the vertical forces, as depicted in Fig. 6(c). Theoretically, the columns are the vertical structure partially submerged in water without lower surface Therefore, only two-component force dynamometer is used to measure the horizontal ISW-forces acting on the columns. The range of the force dynamometer is 9.8 N and the measuring accuracy is 1%. The grooves, in which the bottoms of the columns are placed, are 5 mm deep on each side of the caissons, ensuring that the caissons and columns keep separate. A cylindrical hole with a diameter of 2 cm is made along the central axis of each column, placed the screws connected to the caissons, which allows the screws to remain independent with respect to the columns. The force measuring system designed by this method can not only measure the forces on the columns and caissons separately, but also simulate the coherence characteristics of the flow fields of the columns and caissons as a whole. Better way of change in the incidence angles could be achieved, however, by rotating the test model in the horizontal direction. Moreover, the force measuring system is located sufficiently far from the wave absorber so that any instability, which may occur during the interaction, does not alter the ISW or affect the forces measurement.

Before each experiment, keeping the model in a state of equilibrium is achieved by attaching weights to the measurement system. The measured data are digitized and recorded by the data acquisition system. And the corresponding relationship between the measured electronic signals and loads can be obtained by using the data acquisition system. Then the ISW forces on the columns and caissons of the model can be thus estimated from the electrical signals according to the calibrated relationship, respectively.

4. Results and discussion

A series of experiments were conducted with three different layer thickness ratios ($h_1 : h_2 = 20 : 80, 25 : 75, 30 : 70$), amplitudes and directions of the incident ISWs to obtain the load properties on the columns and caissons of the semi-submersible platform respectively, and the fourth layer thickness ratio $h_1 : h_2 = 35 : 65$ was used for experiments to verify the applicability of the theoretical prediction method. Four propagation directions of ISWs, 0°, 30°, 60° and 90°, were selected for model tests under layer thickness ratio $h_1 : h_2 = 25 : 75$. When the layer thickness ratio $h_1 : h_2 = 20 : 80$ and $h_1 : h_2 = 30 : 70$ were chosen, the experiments were carried out with $\alpha = 90°$, 60° and 30°. And experiment the layer thickness ratio of $h_1 : h_2 = 35 : 65$ was only conducted with 90°. In each propagation direction, nine wave amplitudes of model tests were considered. A total of 99 cases were conducted in the experiments. Typical experimental ISWs under incident angle $\alpha = 90°$ are listed in Table 1. The draft of the model is 0.077 m, and the model is always in the fresh water due to the shallowest upper layer depth of 0.2 m. Two main reasons were taken into account in the selection of the experimental conditions. The fist is to simulate the situation where the semi-submersible platform is always kept in the upper layer fluid in the real ocean. The second is that the experimental conditions contains three different theoretical application ranges. From the table, it is clear that the characteristic length D_e of both columns and caissons is far less than the ISW wavelength, allowing the Morison equation to be used to calculate the wave loads on the model. Morison Equation is a semi-empirical formula based on the diffraction theory with assumption that the structure has no significant effect on the wave propagation, and the additional mass and viscosity of wave play a dominant role in influencing the offshore structures. Therefore, inertia and drag forces are mainly considered in the calculation wave loads by using Morison Equation, without the diffraction force. The key to evaluate the wave load on the small-scale pile by using Morison Equation is to choose the inertia and drag coefficients reasonably.

As obtained from experiments, the selection of two hydrodynamic coefficients C_d and C_m highly correlated with R_e, KC number and the layer thickness ratio in the ISW circumstances. Usually the definition of R_e and KC number are given as $R_e = U_{\max} D_e/\nu$ and $KC = U_{\max} T/D_e$ in which $U_{\max}$ is the maximum horizontal velocity of water particle motion in one wave period, T is the wave period of the ISW and ν is the viscosity coefficient.

The points described here in Fig. 7 represent the variation of the experimental values of the drag coefficient of columns C_{dco} with R_e under different cases. The drag coefficient C_{dco} decreases with increasing R_e in exponential function for three different layer thickness ratios, and the layer thickness ratios have negligible effect upon the drag coefficient. The scatter diagram of the inertia coefficient of the columns C_{mco} is also plotted in Fig. 7. From the figure, it is clearly

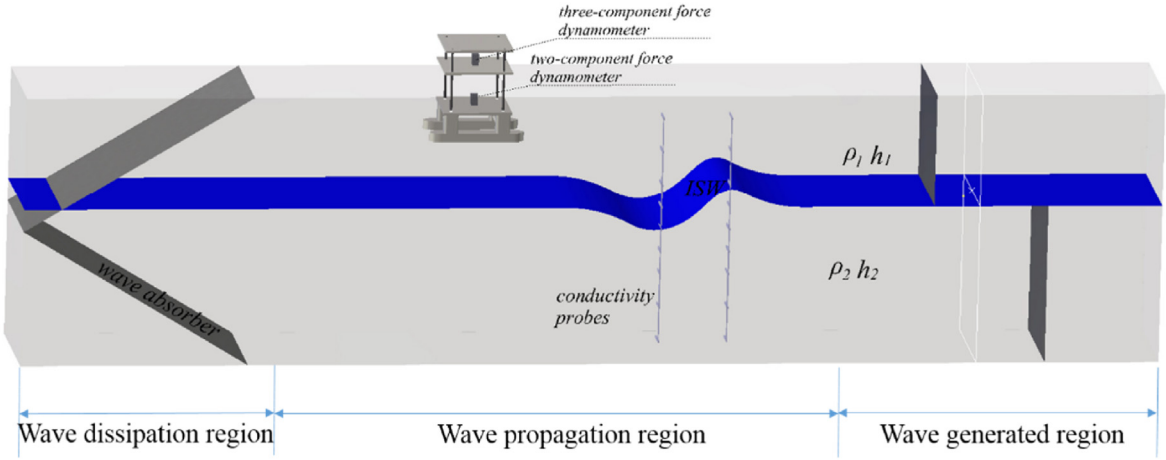

Fig. 4. Sketch of experimental set-up.

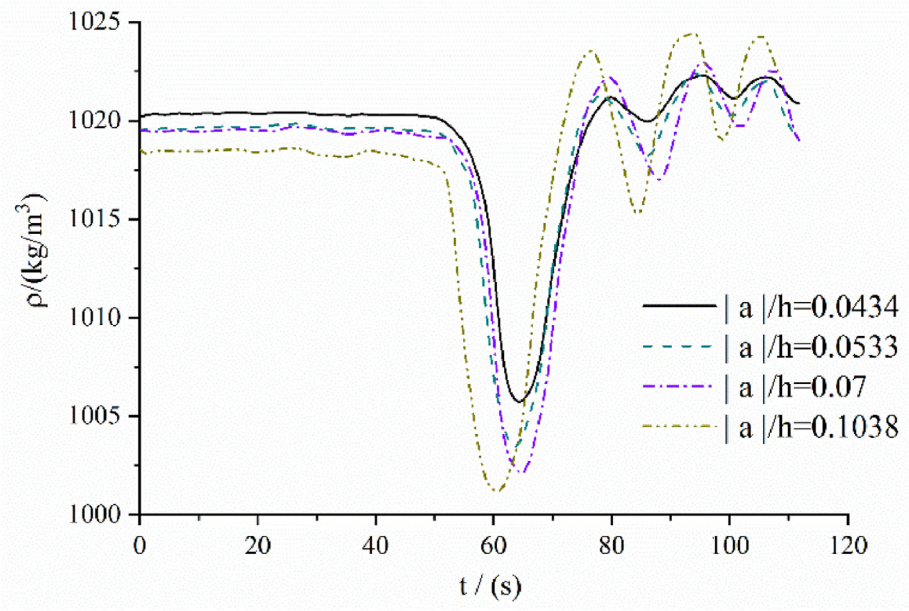

Fig. 5. ISW waveform under different incident amplitudes for. $h_1 : h_2 = 20 : 80$

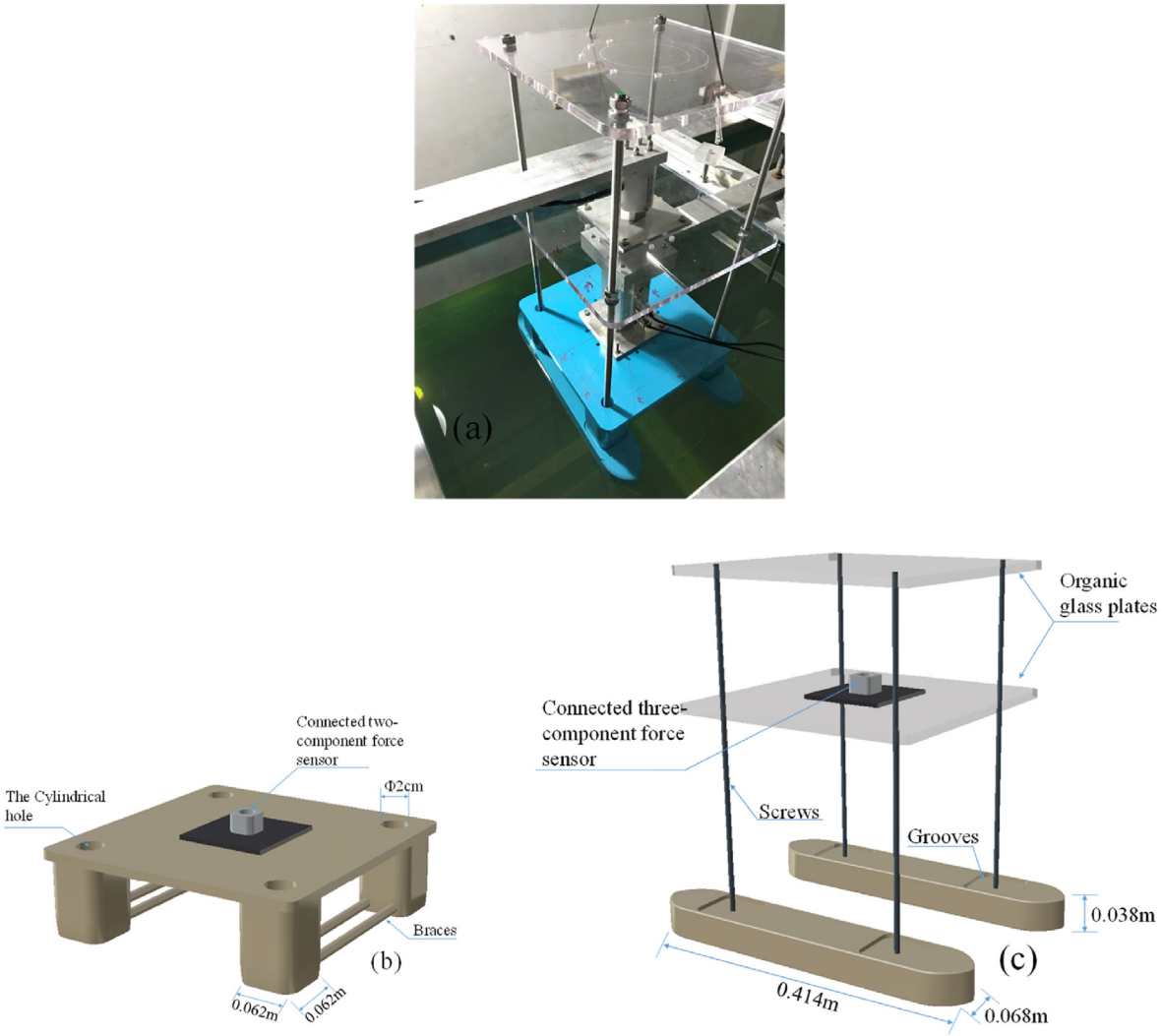

Fig. 6. Experimental model system: (a) installation photo; (b) columns; (c) caissons.

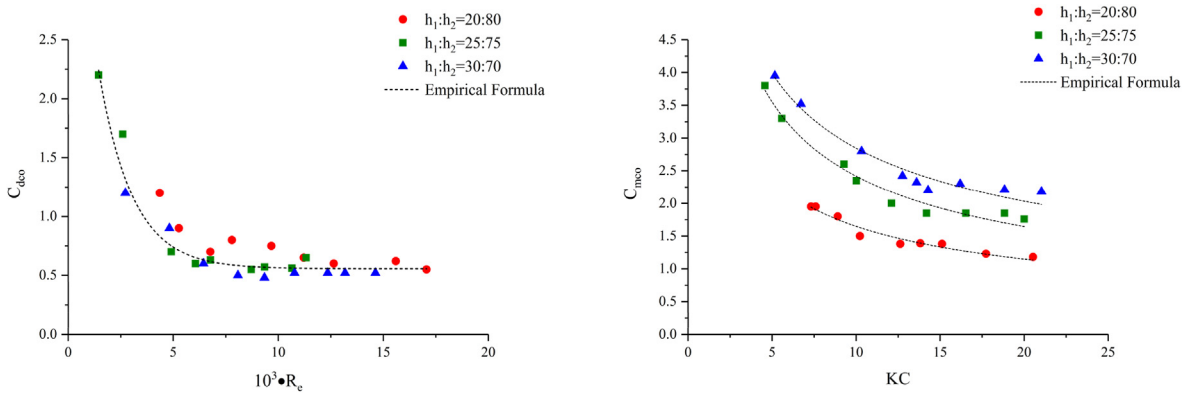

Fig. 7. Experimental results of the drag and inertia coefficients for columns when $\alpha = 90°$.

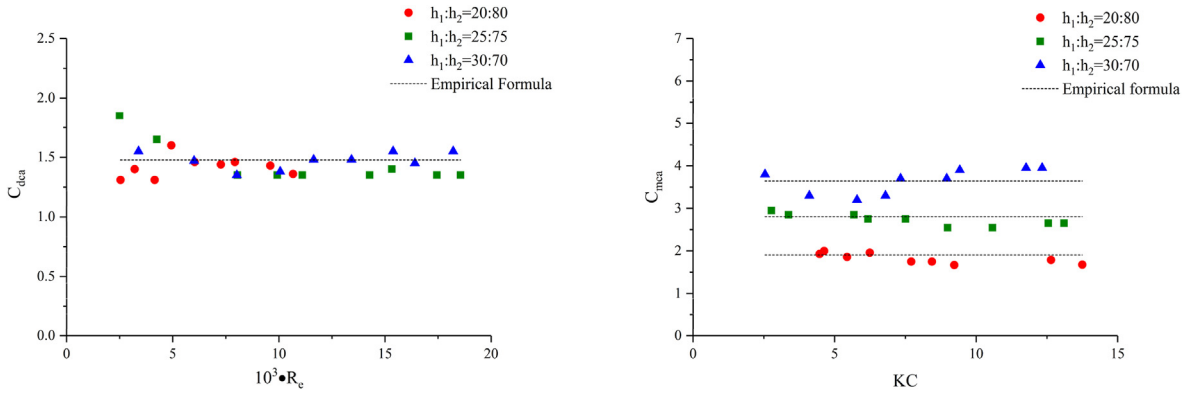

Fig. 8. Experimental results of the drag and inertia coefficients for caissons when $\alpha = 90°$.

seen that C_{mco} mainly depends on the KC number in power function, and decreases as KC increases. Unlike the drag coefficient, C_{mco} is not only related to the KC number, but also to the upper layer depths h_1/h. The appropriate curves can be determined through regression analysis to fit the experimental points, as shown in the figures. And the empirical formulas of C_{dco} and C_{mco} can be written as

$$C_{dco} = 4.159 \times \exp\left(-6.24 \times 10^{-4} \times R_e\right) + 0.556$$
$$C_{mco} = 7.6 \times KC^{\left(\frac{0.37h_1}{h} - 0.6\right)} \tag{21}$$

The relationship between the drag coefficient of the caissons C_{dca} and KC number is figured out through comparative analysis. An interesting feature of C_{dca} can be exhibited, which is different from that of the columns, that is the coefficient is nearly close to the constant under different layer thickness ratios. The reason for the difference of the relationship is that the submerged forms of the columns and caissons in water are different. The columns are the vertical columnar structures partially immersed in water, while the caissons are the horizontal structures completely submerged in water. The measured inertia coefficient of the caissons C_{mca} for these tests is shown in Fig. 8, in which the values of C_{mca} depends

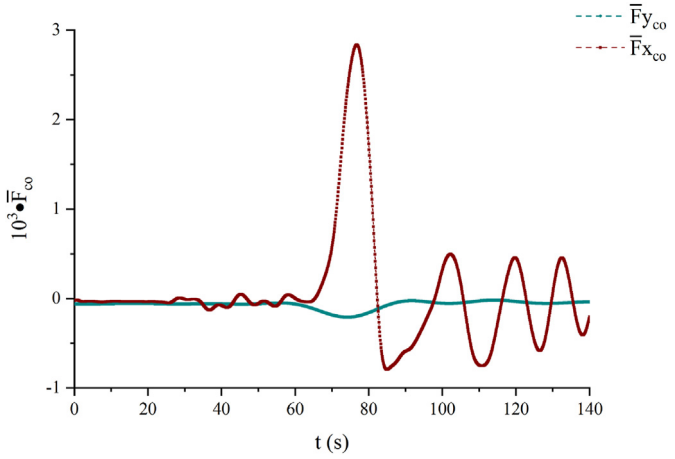

Fig. 9. Comparison of the theoretical and experimental results for time histories of dimensionless ISW-forces exerted on the columns when $\alpha = 60°$ and $\alpha = 30°$.

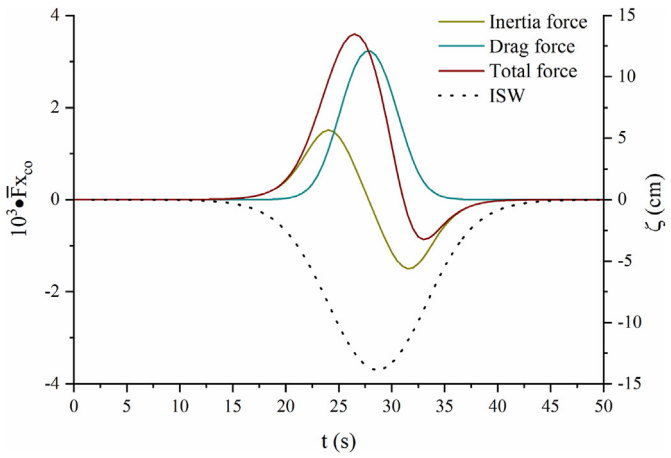

Fig. 10. Comparison of the calculated inertial and drag forces on the columns for h_1: h_2 = 20:80, |a|/h = 13.86, $\alpha = 90°$.

upon the layer thickness ratios and increase with the increase of the upper layer depths h_1/h. From the regression analysis, the empirical formulas of C_{dca} and C_{mca} can be obtained from the experimental data fitting, as

$$\begin{aligned} C_{dca} &= 1.478 \\ C_{mca} &= 0.483*\exp\left(6.48*\frac{h_1}{h}\right) \end{aligned} \tag{22}$$

Based on the established calculation methods of the drag and inertia coefficients, the ISW-loads acting on the columns and caissons can be calculated respectively while the applicability conditions of ISWs theories are taken into account.

4.1. The ISW-Loads on columns of the platform

The horizontal ISW-force acting on the columns along the transversal direction of the flume is seen to be quite small compared to that on the longitudinal part in the experiments (shown in Fig. 9) and, hence, is ignored in the subsequent calculations.

To facilitate discussion, the horizontal force is written in dimensionless form as follows, of which the direction is the same as the positive direction of the ox-axis.

$$\overline{Fx}_{co} = \frac{Fx_{co}}{(\rho_1 g S x_{co} d)} \tag{23}$$

where Sx_{co} denotes the immersed windward area of the columns, d is the draft of the model.

The calculation of forces acting on the columns by the Morison equation are further illustrated. The comparison of each components of the drag and inertia force in the Morison equation are shown in Fig. 10 (For the case h_1: $h_2 = 20{:}80$, $|a|/h = 13.86$, $\alpha = 90°$).

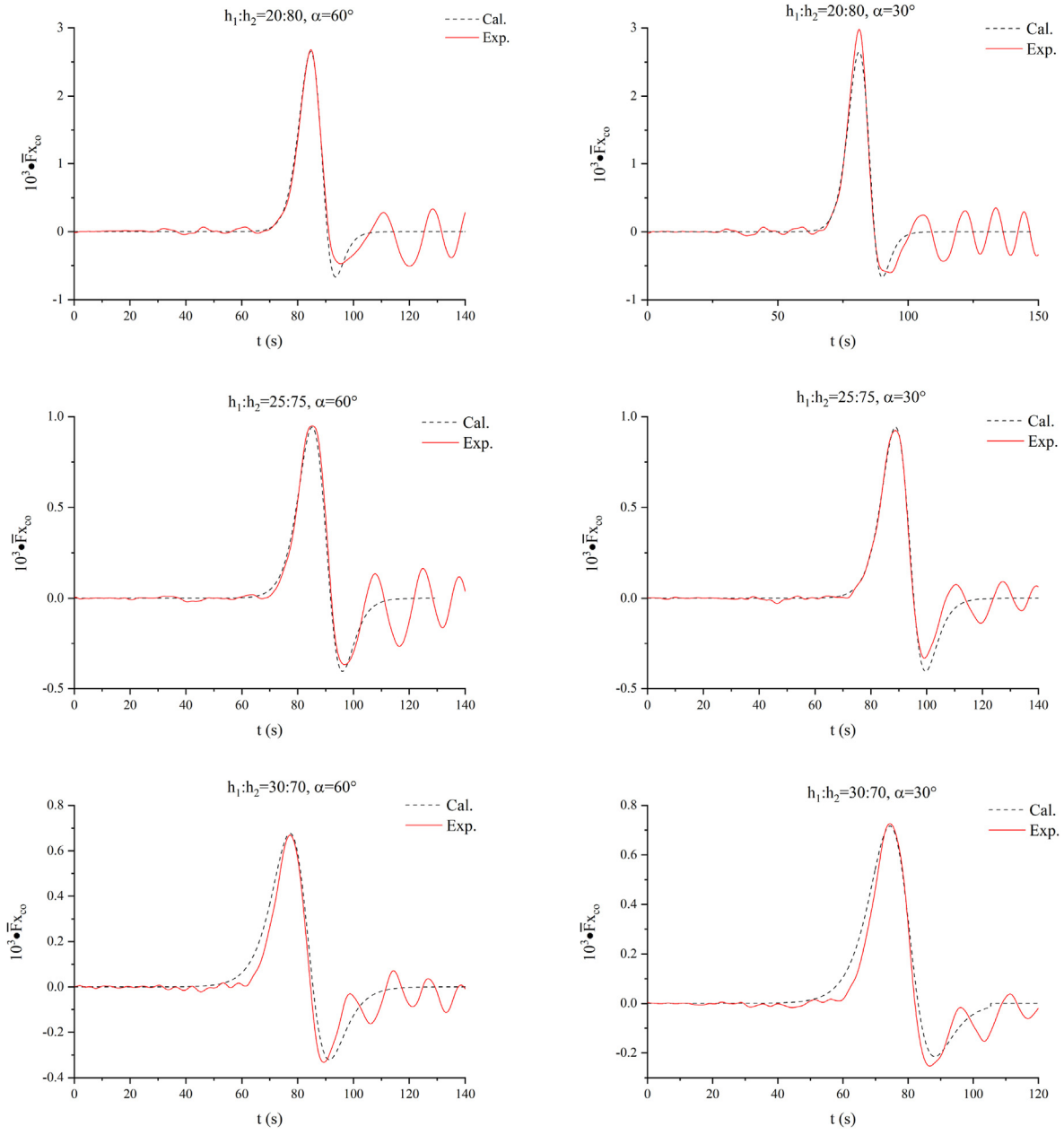

Fig. 11. Comparison of the theoretical and experimental results for time histories of dimensionless ISW-forces exerted on the columns when $\alpha = 60°$ and $\alpha = 30°$.

From the figure, a marked difference in the values as well as the trend of the two forces is observed over the wave period. It is also observed that the peak of the inertia force appears at the rising period of ISW-amplitude, while the drag force peak corresponds to the occurrence of the ISW trough. This signifies that there is a phase difference between the two forces. Moreover, the drag contribution is generally quite a lot to the maximum value of the total force and, the valley value of the total force is dominated by the inertia force.

Fig. 11 shows the characteristics of both the calculated and measured loads on the columns under different layer thickness ratios for incident angle $\alpha = 60°$ and $\alpha = 30°$. The ISW-forces obtained by experiment and calculation show a good agreement, except for some minor differences in the values at force peak and valley. Such difference can be explained by that the energy dissipation is not considered in the calculation. There is always trailing-waves phenomenon behind the leading wave under the experimental conditions, implying the dissipation of wave energy during the ISW generation. It is noticed from the figure that the value of wave-induced forces in experiments tends to change with time. It firstly increases and reaches its maximum. Then the value of wave-induced forces decreases with the ISW propagation. The value of wave-induced forces finally fluctuates around zero after the minimum appears. This can be attributable to the phase difference in the drag and inertia forces. After the minimum occurs, the force on the columns is mainly caused by the inertia force rather than the drag force at this moment. Meanwhile, the value of wave-induced forces obtained in experiments shows a fluctuating trend around zero due to the tailing wave trains as the ISW propagates. Due to the condition of the wave-maker, the tailing wave generated in the experiments are irregular. Compared with the forces induced by the leading soliton, however, the forces induced by the tail wave trains are obviously smaller. Moreover, the theoretical method is not applicable to predict the forces acting on the columns exerted by the tail wave trains.

A comparison of the experimental and theoretical results for incident angle $\alpha = 90°$ is displayed in Fig. 12. And the effects of the amplitudes and layer depths on the horizontal forces of the columns are also demonstrated here. In the figure, the non-dimensional maximum and minimum of the loads is shown as a function of amplitudes $|a|/h$ under three different layer thickness ratios. It is observed that both the maximum and minimum horizontal forces basically increase linearly with the amplitudes and the proportionality coefficients of the maximum forces are closely related to the layer thickness ratios, whereas the minimum forces are almost unaffected by its relative position to the interface between the upper and lower layer. Moreover, similar results are captured by experiments and calculation with three different layer thickness ratios, except for some minor differences in the values, especially at higher wave amplitudes. The horizontal forces from experimental data are slightly higher than the calculated ones, with a magnitude of less than 15%. Possibly, the experimental condition and operation lead to such difference. During the experiment, experiments of the ISWs with small amplitudes are always firstly carried out for each layer thickness ratio. With the experiments undertaken, the obvious mixing behavior appears at the interface between the two layers, which is different from the assumption of the two-layer system. As a consequence, relatively large error is observed here. In addition, the calculation of the forces on the columns by Morison equation without considering the wave scattering effect from the submerged part of the structure may also give

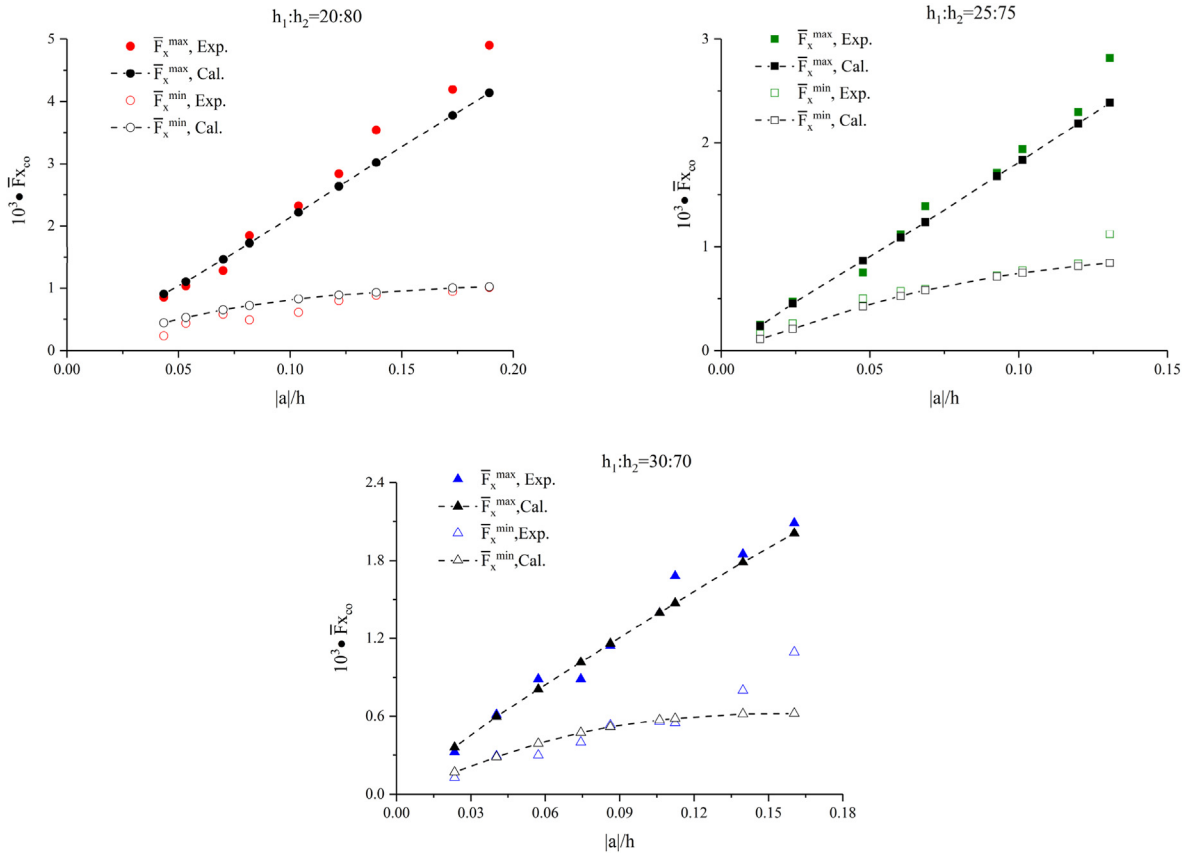

Fig. 12. Comparison of the non-dimensional theoretical and experimental forces for the columns vs. amplitudes under different layer thickness ratios when $\alpha = 90°$.

rise to the differences between the experimental and computed results.

To demonstrate the effects of the incoming wave direction on the forces exerted on the columns and the applicability of the prediction method, three additional groups of experiments were conducted for incidence angel being 60°, 30° and 0° under layer thickness ratio h_1:h_2 = 25:75. Theoretically, the submerged parts of the columns are regular structures and the windward areas remain nearly unchanged during the experiments. Thus, the change of the incoming wave direction in these cases has little influence on the horizontal forces exerted on the columns. This is further verified in Fig. 13 with the comparison of calculations and experiments of the horizontal forces on the columns under different incident angles of interest. It is observed that the maximum and minimum non-dimensional forces exhibit the similar values in the different incidence angles for both experiment and calculation. The horizontal forces obtained by experiment and calculation show a similar increasing trend, except for some minor differences in the values. And the difference shares a same reason with that for incidence angle being 90°.In general, the prediction method of the forces on the columns appears to be satisfied in the ISWs environments, and the empirical formulas of C_{dco} and C_{mco} established from the experiments are reasonable here.

4.2. The ISW-Loads on caissons of the platform

4.2.1. The horizontal ISW-loads on the caissons

The total horizontal forces can be generally divided into three components: the velocity force (the drag force), acceleration related force (the inertia force) and differential pressure (the Froude-Krylov force). For the cases where the incoming wave is not parallel to the longitudinal profile, the drag and inertia force components are usually deemed as the major part of the total force. However, the Froude-Krylov force is used to appropriately predict the horizontal forces at the incident angle being 0°.Unlike the cases of the columns observed, the horizontal ISW-forces along the transversal direction of the flume acting on the caissons could not be neglected in the subsequent analysis. First, denoted $\overline{Fx}_{cai}$ and $\overline{Fy}_{cai}$, simply represent the non-dimensional horizontal transversal and longitudinal forces respectively and are defined as follows

$$\overline{Fx}_{cai} = \frac{Fx_{cai}}{\rho_1 g S_{cai}^{3/2}}, \quad \overline{Fy}_{cai} = \frac{Fy_{cai}}{\rho_1 g S_{cai}^{3/2}} \tag{24}$$

where, S_{cai} is the immersed windward area of the caissons.

The comparisons between the predicted and experimental peak results under three different layer thickness ratios for $\alpha = 90°$ are typically demonstrated in Fig. 14. The characteristics of the forces are similar to the observations as discussed above for the columns and hence, they are not further addressed here. Similar to the columns, the non-dimensional horizontal forces are linearly proportional to the amplitudes, and the proportionality coefficients of the maximum forces are closely related to the layer thickness ratios. It is also interestingly noticed that the closer to interface, the larger horizontal forces on both columns and caissons. The possible reason is the gravitational influence of the upper layer fluid on the ISW flow field. The figures also indicate that the computations are in close agreement with the experimental results, the maximum deviation being about 15%.

In order to further verify the application of the prediction

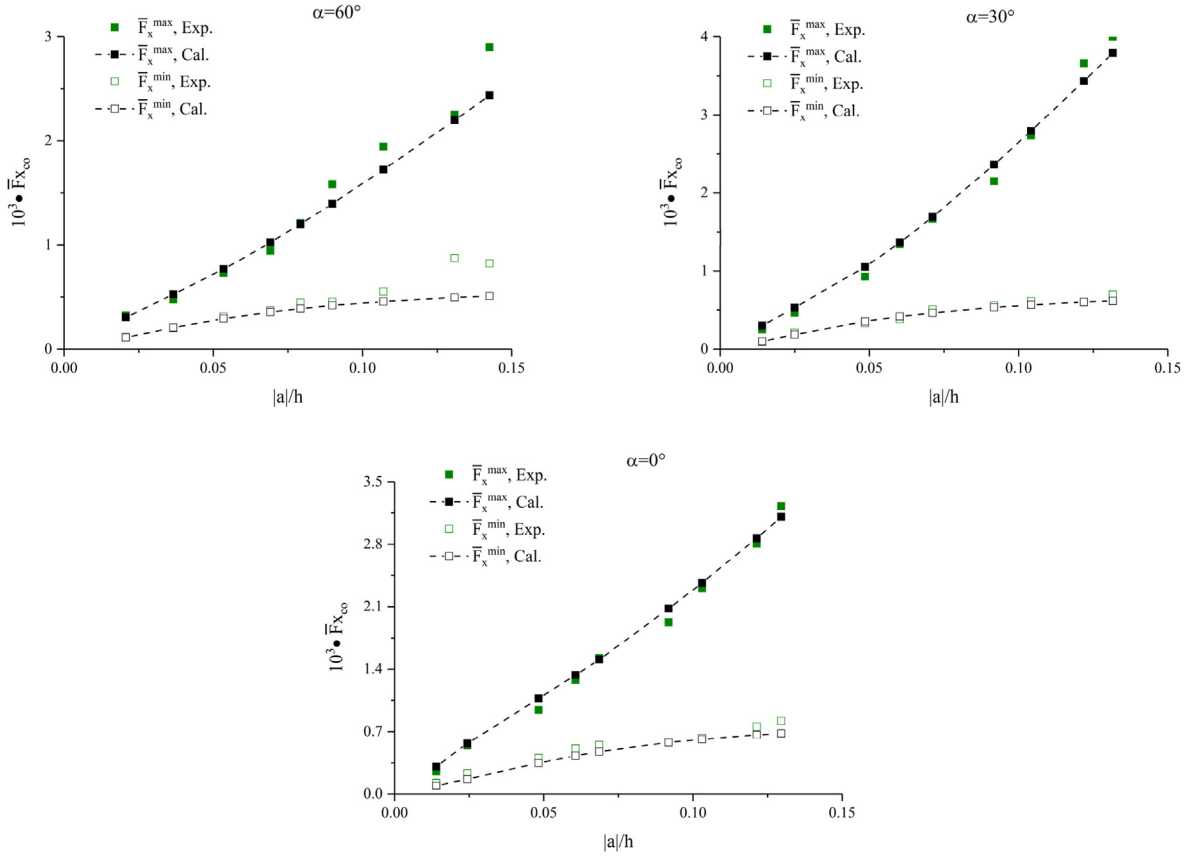

Fig. 13. Comparison of the non-dimensional theoretical and experimental forces for the columns vs. amplitudes under different incident angles when h_1:h_2 = 25:75.

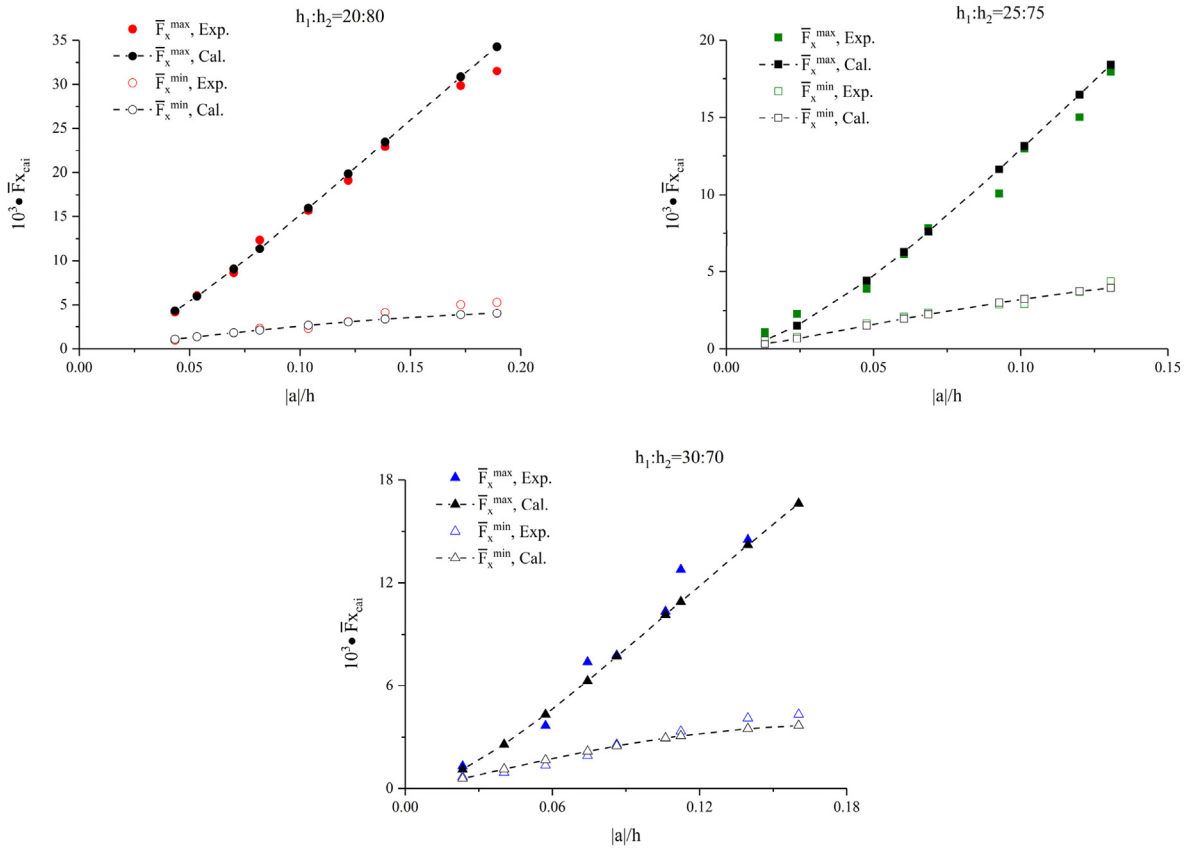

Fig. 14. Comparison of the non-dimensional theoretical and experimental forces for the caissons vs. amplitudes under different layer thickness ratios when $\alpha = 90°$.

method, a series of experiments were conducted under layer thickness ratio $h_1{:}h_2 = 35{:}65$. The obtained non-dimensional horizontal forces for the incident angle of 90° are plotted in Fig. 15, where the results of experiments are also shown here. The theoretical results are calculated by the empirical formula (Eq. (22)) obtained from the first three groups of experiments. It is observed that the theoretical prediction results are in good agreement with the experimental results. It can be proved that the theoretical method obtained in this paper can effectively predict the loads acting on the semi-submersible platform induced by ISWs.

To further verify the application of the prediction method and the influence of the incoming wave on the horizontal forces, two more different incident angles are considered. The obtained non-dimensional horizontal transversal and longitudinal forces for different incident angles are plotted in Fig. 16, where the results of experiments are also shown here. It is observed from the figures that the effect of the incoming wave directions has remarkable influence on the horizontal forces, different from the cases of columns. And the relatively complex projected area and the shielding effect account for the effect. The details of the differences between the predicted ones by the modified Morison equation and the experimental results are observed in the figures. The reason for this phenomenon is believed that the complex interaction of the ISW-forces and caissons may not be guaranteed to be perfectly represented by the approximate coefficients considered. However, although the proposed calculation method exist slightly differences

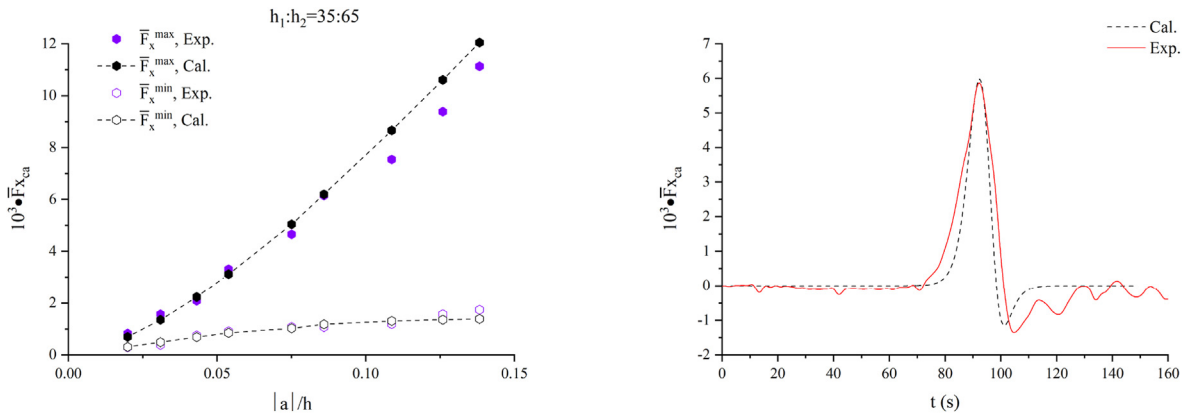

Fig. 15. Comparison of the non-dimensional theoretical and experimental forces for the caissons vs. amplitudes for $h_1{:}h_2 = 35{:}65$.

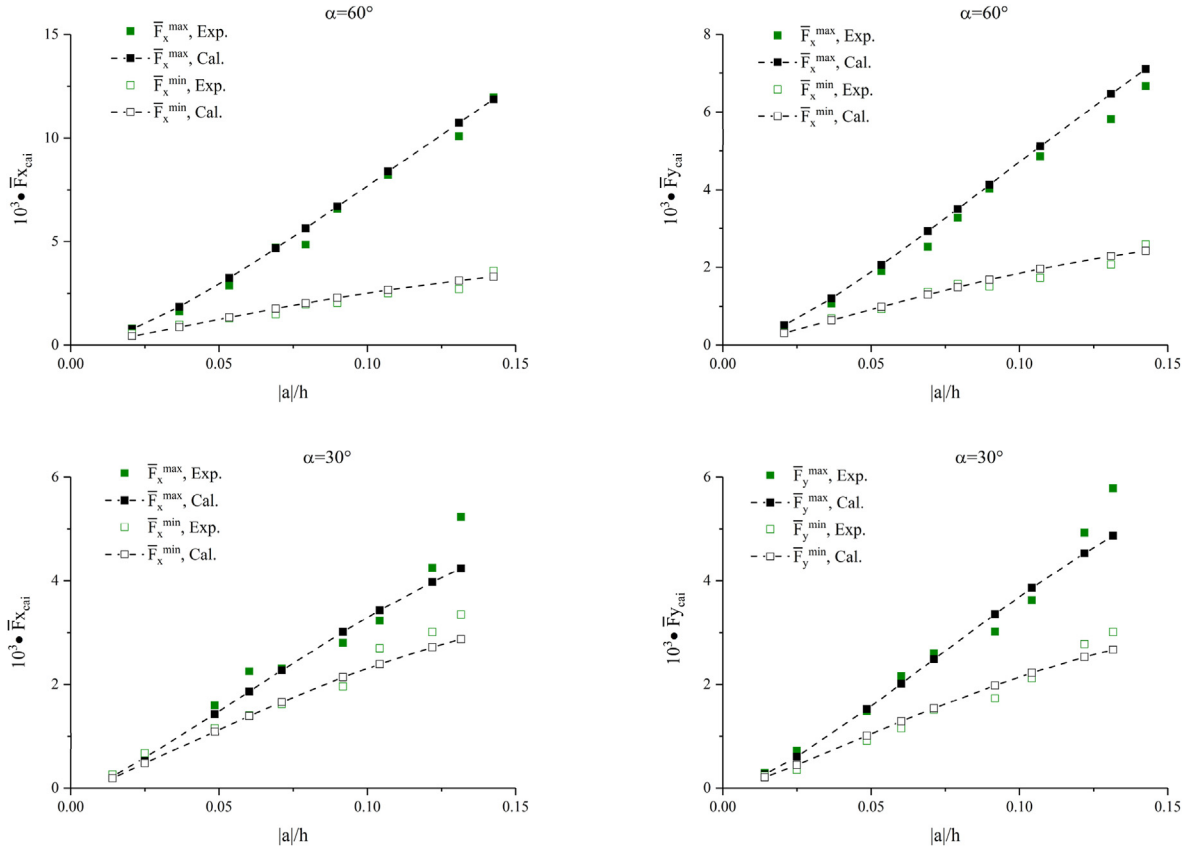

Fig. 16. Comparison of the non-dimensional theoretical and experimental forces for the caissons vs. amplitudes under different incident angles when h_1:h_2 = 25:75.

relative to the experimental forces, the maximum error is no more than 15%, indicating that the calculated method predicts close results of the horizontal forces on the caissons when the incoming wave is not parallel to the longitudinal profile of the platform.

The comparisons of the horizontal forces between the experimental results and those predicted by the Froude-Krylov method for incident angle being 0° are plotted in Fig. 17. The horizontal forces linearly increase with the increase in the amplitudes. The calculated results show a good agreement with the measurements, and the error is less than 10%. It is also interestingly noticed that the peak and valley values of the non-dimensional horizontal forces are the same for each amplitude of ISW due to the symmetrical test model, which is different from the cases that the total force is mainly caused by the drag and inertia components. Whereas the minimum values of the horizontal forces are less than the maximum in the experiments. This is because there exists slight separate of flow at the back of the model due to the fluid viscosity. In summary, good and substantial agreements are observed in this verification, further ensuring that the Froude-Krylov method can make successful predictions of the ISW-forces in the horizontal direction when the incoming wave is parallel to the longitudinal profile of the platform.

4.2.2. The vertical ISW-loads on the caissons

The change of the dynamic pressure in the flow field caused by the ISW propagation seems to determine the vertical force acting

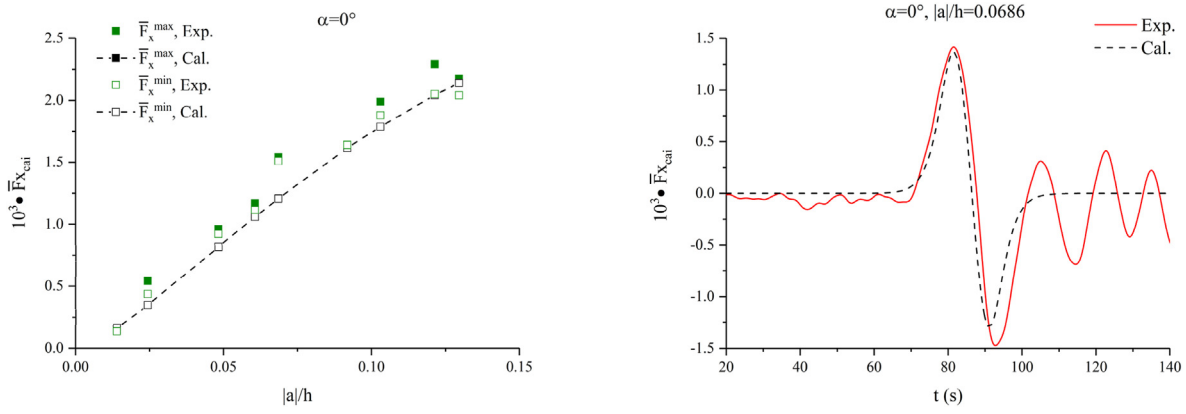

Fig. 17. Comparison of the non-dimensional theoretical and experimental forces for the caissons under incident angle $\alpha = 0°$ when h_1:h_2 = 25:75.

on the caissons, which can be obtained by Eq. (19) while the effects of the structures on the characteristic of ISWs are neglected. The following formula gives a relation of the vertical force in the non-dimensional form:

$$\overline{Fz}_{cai} = \frac{Fz_{cai}}{\rho_1 g S z_{cai}^{3/2}} \tag{25}$$

where Sz_{cai} denotes the wetted surface area of the caissons in z direction.

Fig. 18 presents the time histories of vertical force profiles of both measurement and calculation under three different layer thickness ratios for incident angle $\alpha = 90°$. The value of vertical forces increases as time evolves before the internal soliton reaches the center axis of the model. Its peak value appears when the ISW passes through the model, and then the value decreases. The dimensionless vertical forces of both methods follow the same general trend over time except for some tail oscillations in the experimental curve, which is the same as the horizontal forces. The vertical force is purely positive pointing upwards due to the semi-submersible model always keeping in the upper layer fluid, where the direction of the horizontal velocity induced by the ISW flow field is the same as that of wave propagation. However, it can still be observed that slight oscillations occur after internal soliton after passed the model in the experiment, resulting in a negative value of the vertical forces.

Using the verified methodology, a demonstration of the characteristics of the vertical forces with amplitudes considering different layer thickness ratios and incoming wave directions are presented in Fig. 19. Note that the changes of incident angles create insignificant variations on the non-dimensional vertical loads, as assumed. It is also in the figures noteworthy that small differences in the peak values of the vertical forces under the different layer thickness ratios are found; that is to say, the non-dimensional vertical forces are almost unaffected by the stratification, which is attributed to that the ISW-induced velocity in the upper layer fluid remains nearly unchanged along the vertical direction of the water depth. Unlike the horizontal forces, the vertical forces vary non-linearly with amplitudes of the wave. There is an overall agreement in the results between the theoretical calculation and model test data, except for several cases caused by the stratified fluid mixing. In general, good agreements are obtained in the verification of the vertical forces on caissons, which proves that the prediction of the ISW-vertical forces used by Froude-Krylov formula is reasonable.

In summary, during the propagation of ISWs, not only the horizontal forces act on the platform but also the vertical forces. Under the action of waves, the responses of the semi-submersible platform in surge and heave motions induced by horizontal and vertical forces have a significant impact on the safety of mooring system.

5. Conclusions

ISWs have much greater amplitudes than their surface counterparts, generating huge wave forces and causing severe damages to the platforms. In this paper, a method for predicting ISW-forces on columns and caissons of the semi-submersible platform is established. Based on the comparisons between the experimental results and those acquired through Morison equation and pressure integral, the appropriateness of the calculation method in predicting the ISW-forces is examined, and the effect of the incoming wave direction on the ISW-forces is also studied. Meanwhile, the applicable formulas of drag and inertia coefficients in the Morison

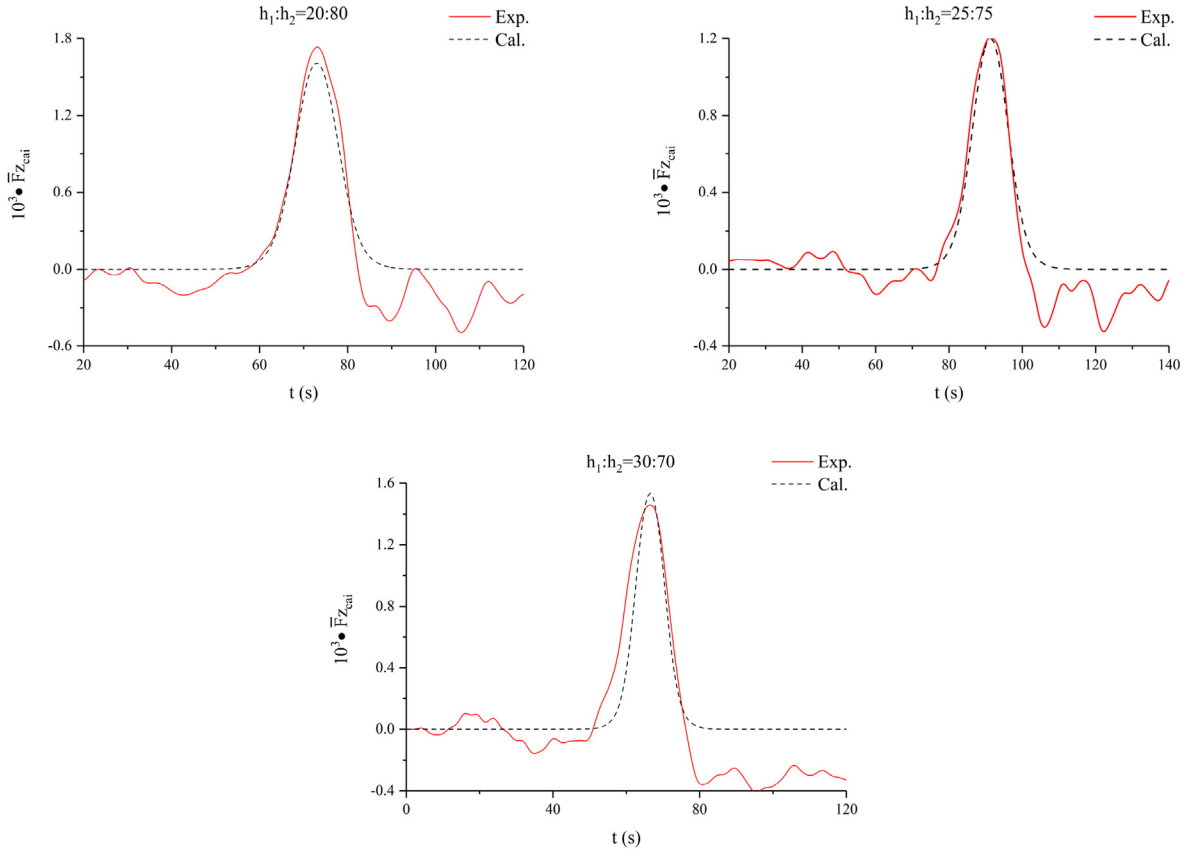

Fig. 18. Comparison of the theoretical and experimental results for time histories of dimensionless vertical forces exerted on the caissons when $\alpha = 90°$.

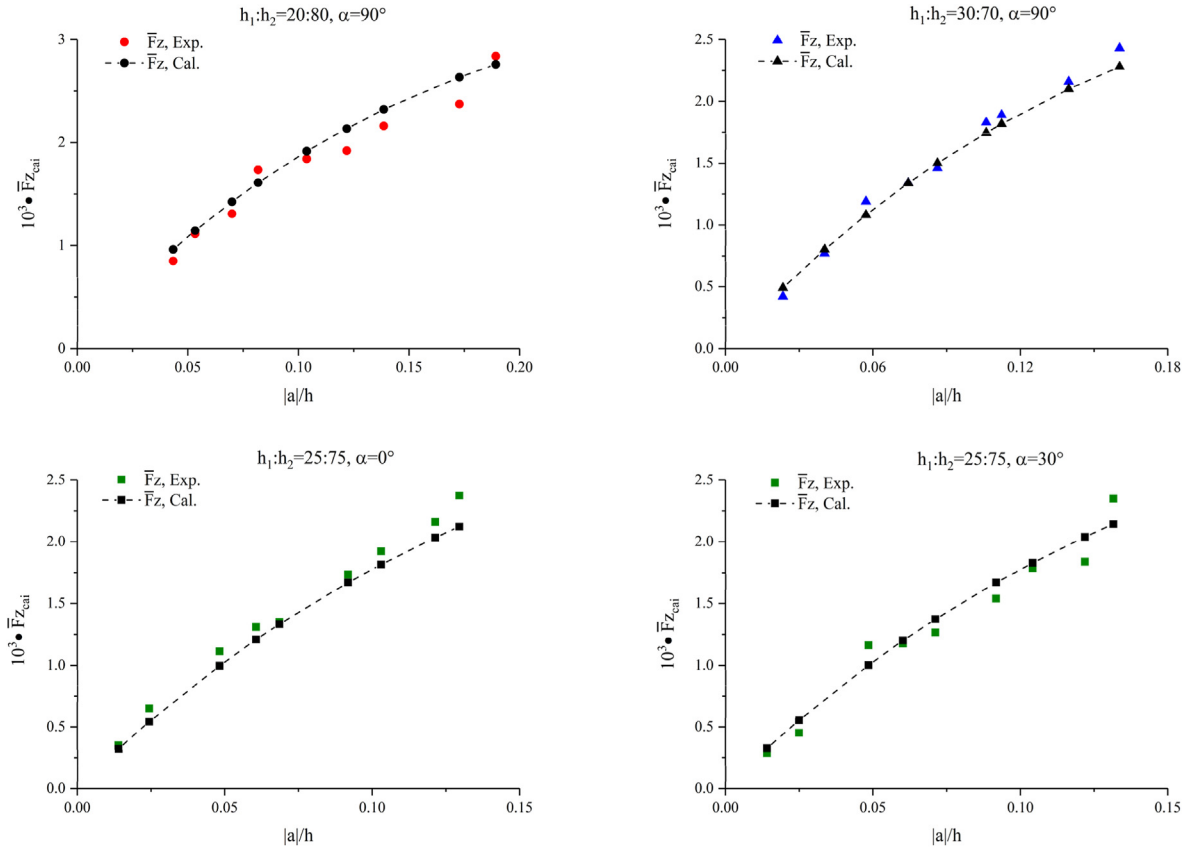

Fig. 19. Comparison of the non-dimensional theoretical and experimental vertical forces for the caissons vs. amplitudes under different incident angles and layer thickness ratios.

Table 1
Conditions in experiments.

h_1:h_2	a (cm)	L(m)	D_{ecol}/L	D_{ecai}/L
20:80	4.34, 5.33, 7.00, 8.18, 10.38, 12.18, 13.86, 17.28, 18.92	2.97–4.05	0.031–0.042	0.051–0.069
25:75	1.31, 2.40, 4.77, 6.03, 6.86, 9.27, 10.13, 12.00, 13.06	4.13–5.66	0.022–0.03	0.036–0.05
30:70	2.34, 4.04, 5.72, 7.44, 8.62, 10.61, 11.24, 13.97, 16.04	5.29–7.30	0.017–0.024	0.028–0.039
35:65	1.99, 3.10, 4.32, 5.39, 7.51, 8.60, 10.87, 12.60, 13.83	5.68–8.82	0.014–0.022	0.024–0.037

equation for the columns and caissons, introduced through the experimental determination of ISWs loads, are given here.

The drag coefficient of columns decreases with increasing Re number in exponential function $C_{dco} = 4.159 \times \exp(-6.24 \times 10^{-4} \times R_e) + 0.556$, while the inertia coefficient of columns decreases with KC number in power function $C_{mco} = 7.6 \times KC^{(0.37h_1/h-0.6)}$; the drag coefficient of caissons is approximately constant $C_{dca} = 1.478$ and the inertia coefficient of caissons varies with layer thickness ratios in exponential function $C_{mca} = 0.483 \times \exp(6.48 \times h_1/h)$

The study indicates that the results of the computation method are in close agreement with the experimental data of both columns and caissons. This suggests that the Morison equation can be applied to analyze the ISW-horizontal forces exerted on the columns, whilst Morison equation is allowed to calculate the horizontal forces on the caissons when the direction of incoming waves is not parallel to the longitudinal profile of the platform; the horizontal forces on the caissons, if the incoming wave is in the same direction with the longitudinal profile, can be analyzed by means of the Froude-Krylov approach. However, the Froude-Krylov equation can be used to estimate the vertical ISW-load regardless of the propagation direction of the ISWs. Furthermore, the vertical force is not exactly linearly proportional to the wave amplitude.

It is also found that the maximum horizontal force on either columns or caissons always increases with the layer thickness ratios decreasing; however, the influence of the layer thickness ratio on both minimum horizontal and vertical forces is relatively limited. In addition, the incoming wave direction may also contribute greatly to the values of horizontal forces exerted on the caissons, which can be ignored in the vertical force analysis when the influential factors are considered.

Overall, this prediction method would serve as a convenient way to give a reasonable and feasible estimation of the ISW-forces on similar kinds of semi-submersible platforms.

At present, this article is based on the experiments, hoping to clarify the formation mechanism of ISW-loads components, verify the applicability of the simplified calculation method for engineering. Explorations of the scale-effect details and influencing factors can be pursued in the future research.

Funding

This research was funded by the National Natural Science Foundation of China, grant No. 11802301 and No. 11802176.

Declaration of competing interest

The authors declare that they have no known competing financial interests or personal relationships that could have appeared to influence the work reported in this paper.

References

Bole, J.B., Ebbesmeyer, C.C., Romea, R.D., 1994. Soliton currents in the South China sea: measurements and theoretical modeling. OTC 7417. In: 26th Annual Offshore Technology Conference, pp. 367–376. Houston, Texas. https://www.onepetro.org/download/conference-paper/OTC-7417-MS?id=conference-paper%2FOTC-7417-MS.

Cai, S., Long, X., Gan, Z., 2003. A method to estimate the forces exerted by internal solitons on cylindrical piles. Ocean Eng. 30, 673–689. https://www.sciencedirect.com/science/article/pii/S0029801802000380.

Cai, S., Wang, S., Long, X., 2006. A simple estimation of the force exerted by internal solitons on cylindrical piles. Ocean Eng. 33 (7), 974–980. https://www.sciencedirect.com/science/article/pii/S0029801805001940.

Cai, S., Long, X., Wang, S., 2008. Forces and torques exerted by internal solitons in shear flows on cylindrical piles. Appl. Ocean Res. 30 (1), 72–77. https://www.sciencedirect.com/science/article/pii/S0141118708000138.

Camassa, R., Choi, W., Michallet, H., Rusas, P.O., Sveen, J.K., 2006. On the realm of validity of strongly nonlinear asymptotic approximations for internal waves. J. Fluid Mech. 549, 1–23. https://www.researchgate.net/publication/231874141_On_the_realm_of_validity_of_strongly_nonlinear_asymptotic_approximations_for_internal_waves.

CHEN, J.H., 1996. Liuhua 11-1 deep sea oil-field development project in South China Sea. Chin. Offshore Platform 11 (1), 43–45 in Chinese. https://www.ixueshu.com/document/ef4abee81d2fbba9318947a18e7f9386.html.

Chen, C., Hsu, J.R., Cheng, M., 2007. An investigation on internal solitary waves in a two-layer fluid: propagation and refection from steep slopes. Ocean Eng. 34, 171–184. https://www.sciencedirect.com/science/article/pii/S002980180600076X.

Choi, W., Camassa, R., 1999. Fully nonlinear internal waves in a two-fluid system. J. Fluid Mech. 396, 1–36. https://www.sciencedirect.com/science/article/pii/S030193229780359X.

Djordjevic, V.D., Redekopp, L.G., 1978. The fission and disintegration of internal solitary waves moving over two-dimensional topography. J. Phys. Oceanogr. 8 (6), 1016–1024. https://watermark.silverchair.com/1520-0485(1978)008_1016_tfadoi_2_0_co_2.pdf?token=AQECAHi208BE49Ooan9kkhW_Ercy7Dm3ZL_9Cf3qfKAc485ysgAAAvEwggLtBgkqhkiG9w0BBwagggLeMIIC2gIBADCCAtMGCSqGSIb3DQEHATAeBglghkgBZQMEAS4wEQQMrlyhmlSm6quxWlPLAgEQgIICpIpxUeZKA7PgSRA1.

Ebbesmeyer, C.C., Coomes, C.A., Hamilton, R.C., 1991. New observations on internal waves (solitons) in the South China Sea using an acoustic Doppler current profiler. Mar. Technol. Soc. J. 91, 165–175. https://www.onepetro.org/download/conference-paper/OTC-10793-MS?id=conference-paper%2FOTC-10793-MS.

Faltinsen, O., 1993. Sea Loads on Ships and Offshore Structures. Cambridge University Press. http://gen.lib.rus.ec/book/index.php?md5=1C8C62FBB867D15BA95E4B52FB10DD6B.

Goryachkin, Yu N., Ivanov, V.A., Pelinovsky, E.N., 1992. Transformation of internal tidal waves over the Guinean Shelf. Sov. J. Phys. Oceanogr. 3, 309–315. https://link.springer.com/article/10.1007/BF02197307.

Helfrich, K.R., Melville, W.K., 2006. Long nonlinear internal waves. Annu. Rev. Fluid Mech. 38, 395–425. https://www.researchgate.net/publication/33547696_Long_nonlinear_internal_waves_Ann_Rev_Fluid_Mech?ev=auth_pub.

Huang, W.H., You, Y.X., Shi, Q., 2013. The experiments of internal solitary wave load and their theoretical model for a semi-submersible platform. Chin. J. Hydrodynamic. 28 (6), 644–657 in Chinese. http://en.cnki.com.cn/Article_en/CJFDTotal-SDLJ201306002.htm.

Hutter, K., 2012. Nonlinear Internal Waves in Lakes. Springer, Berlin. https://www.researchgate.net/publication/321609998_Nonlinear_Internal_Waves_in_Lakes.

Kakutani, T., Yamasaki, N., 1978. Solitary waves on a two-layer fluid. J. Phys. Soc. Jpn. 45 (2), 674–679. https://journals.jps.jp/doi/abs/10.1143/JPSJ.45.674.

Kao, T.W., Pan, F.S., Renouard, D., 1985. Internal solitons on the pycnocline: generation, propagation, shoaling and breaking over a slope. J. Fluid Mech. 159, 19–53. https://www.cambridge.org/core/services/aop-cambridge-core/content/view/986FC16C6795E0A3DEFBEDCAAACA51E3/S0022112085003081a.pdf/internal_solitons_on_the_pycnocline_generation_propagation_and_shoaling_and_breaking_over_a_slope.pdf.

Koop, C.G., Butler, G., 1981. An investigation on solitary internal waves in a two-fluid system. J. Fluid Mech. 112, 225–251. https://www.cambridge.org/core/services/aop-cambridge-core/content/view/AC886941E613996138907626D7CFC16C/S0022112081000372a.pdf/an_investigation_of_internal_solitary_waves_in_a_twofluid_system.pdf.

Lamb, K.G., 1994. Numerical experiments of internal wave generation by strong tidal flow across a finite amplitude bank edge. J. Geophys. Res. 99, 843–864. http://mseas.mit.edu/download/evheubel/LambJGRO1994.pdf.

Leichter, J.J., Deane, G.B., Stokes, M.D., 2005. Spatial and temporal variability of internal wave forcing on a Coral Reef. J. Phys. Oceanogr. 35 (11), 1945–1959. https://www.proquest.com/docview/223940224?OpenUrlRefId=info:xri/sid:baidu&accountid=13818.

Michallet, H., Barthélemy, E., 1997. Ultrasonic probes and data processing to study interfacial solitary waves. Exp. Fluid 22 (5), 380–386. https://link.springer.com/article/10.1007/s003480050064.

Miyata, M., 1985. An internal solitary wave of large amplitude. La Mer 23, 43–48. https://www.mendeley.com/catalogue/c330be44-305e-3ef3-a530-f6e39d7d6807/.

Morison, J.R., Obrien, M.P., Johnson, J.W., Schaaf, S.A., 1950. The force exerted by surface waves on piles. J. Petrol. Technol. 2 (5), 149–154. https://www.onepetro.org/journal-paper/SPE-950149-G.

Osborne, A.R., Burch, T.L., 1980. Internal solitons in the Andaman sea. Science 208 (4443), 451–460. https://science.sciencemag.org/content/208/4443/451.

Wang, X., Lin, Z.Y., You, Y.X., 2015. Numerical simulation for the load characteristics of internal solitary waves on the semi-submersible platform. J. Ship Mech. 19 (10), 1173–1184 in Chinese. http://en.cnki.com.cn/Article_en/CJFDTOTAL-CBLX201510002.htm.

Wang, S.D., Wei, G., Du, H., Wu, J.L., Wang, X.L., 2020. Experimental investigation of the wave-flow structure of an oblique internal solitary wave and its force exerted on a slender body. Ocean Eng. 201. https://www.sciencedirect.com/science/article/pii/S002980182030130X.

Wessels, F., Hutter, K., 1996. Interaction of internal waves with a topographic sill in a two-layered fluid. J. Phys. Oceanogr. 26 (1), 5–20. https://watermark.silverchair.com/1520-0485(1996)026_0005_ioiwwa_2_0_co_2.pdf?token=AQECAHi208BE49Ooan9kkhW_Ercy7Dm3ZL_9Cf3qfKAc485ysgAAAt0wggLZBgkqhkiG9w0BBwaggg LKMIICxgIBADCCAr8GCSqGSIb3DQEHATAeBglghkgBZQMEAS4wEQQMQ xvclnFf56qkW5xYAgEQgIICkM4a6sOz0vCGLUx6.

Xie, J., Jian, Y., Yang, L., 2010. Strongly nonlinear internal soliton load on a small vertical circular cylinder in two-layer fluids. Appl. Math. Model. 34 (8), 2089–2101. https://www.sciencedirect.com/science/article/pii/S0307904X09003539.

Xie, J., Xu, J., Cai, S., 2011. A numerical study of the load on cylindrical piles exerted by internal solitary waves. J. Fluid Struct. 27 (8), 1252–1261. https://www.sciencedirect.com/science/article/pii/S0889974611000697.

You, Y.X., Li, W., He, J.Y., 2010. Hydrodynamic characteristic of tension leg platforms in ocean internal solitary waves. J. Shanghai Jiao Tong Univ. (Sci.) 44 (1), 12–17 in Chinese. http://en.cnki.com.cn/Article_en/CJFDTOTAL-SHJT201001013.htm.

You, Y.X., Li, W., Hu, T.Q., 2012. Dynamic responses of a semi-submersible platform in internal solitary waves. Ocean Eng. 30 (2), 1–7 in Chinese. http://en.cnki.com.cn/Article_en/CJFDTOTAL-HYGC201202002.htm.

Zhang, W.G., Duda, T.F., Udovydchenkov, A.A., 2014. Modeling and analysis of internaltide generation and beamlike onshore propagation in the vicinity of shelf break Canyons. J. Phys. Oceanogr. 44, 834–849. https://www.proquest.com/docview/1509068715?OpenUrlRefId=info:xri/sid:baidu&accountid=13818.